Wideband Electrically Pumped 1050-nm MEMS-Tunable VCSEL for Ophthalmic Imaging

Demis D. John, *Member, IEEE*, Christopher B. Burgner, Benjamin Potsaid, Martin E. Robertson, Byung Kun Lee, Woo Jhon Choi, Alex E. Cable, James G. Fujimoto, *Fellow, IEEE*, and Vijaysekhar Jayaraman, *Member, IEEE*

Abstract—In this paper, we present a 1050-nm electrically pumped microelectromechanically tunable vertical cavity surface-emitting laser (MEMS-VCSEL) with a record dynamic tuning bandwidth of 63.8 nm, suitable for swept-source optical coherence tomography (SS-OCT) imaging. These devices provide reduced cost and complexity relative to previously demonstrated optically pumped devices by obviating the need for a pump laser and associated hardware. We demonstrate ophthalmic SS-OCT imaging with the electrically-pumped MEMS-VCSEL at a 400 kHz axial scan rate for wide-field imaging of the *in vivo* human retina over a 12 mm × 12 mm field and for OCT angiography of the macula over 6 mm × 6 mm and 3 mm × 3 mm fields to show retinal vasculature and capillary structure near the fovea. These results demonstrate the feasibility of electrically pumped MEMS-VCSELs in ophthalmic instrumentation, the largest clinical application of OCT. In addition, we estimate that the 3 dB coherence length in air is 225 ± 51 m, far greater than required for ophthalmic SS-OCT and suggestive of other distance ranging applications.

Index Terms—Medical imaging, micro and nano opto-electro-mechanical systems (MOEMS), optical coherence tomography, semiconductor lasers, tunable lasers.

Fig. 1. Schematic of the electrically-pumped MEMS-VCSEL with a p-i-n diode structure, intrinsic MQW and oxidized AlGaAs layers on an n-type GaAs substrate.

I. INTRODUCTION

THE wide wavelength tuning range, rapid tuning rate, and long coherence length of recently developed vertical cavity surface emitting lasers with micro-electromechanical systems-based tuning mechanisms (MEMS-VCSELs) has made these optical sources an attractive technology for swept-source optical coherence tomography (SS-OCT) [1]. Optically pumped MEMS-VCSEL light sources have been demonstrated in SS-OCT systems with variable imaging rates up to 1 MHz [2], axial resolution of 9 μm [3], record centimeter range imaging of large objects, full eye-length measurements, optical fiber measurement greater than 1 m [3], [4], and hand-held OCT [5]. SS-OCT

used in ophthalmology can prevent irreversible vision-loss by enabling early detection and monitoring of ocular disease in a non-invasive manner. In ophthalmology, the long coherence length combined with the variable and high speed imaging capabilities of the previously described optically pumped 1050 nm MEMS-VCSEL [6] has enabled new OCT capability, such as multipurpose instrumentation that can image the retina and anterior eye, and perform full eye length measurement [3], enface Doppler blood flow measurement techniques with rapidly repeated volumes to visualize pulsatility [7], and densely sampled dye-free OCT angiography (OCTA) [8].

Transitioning from an optically-pumped MEMS-VCSEL system as in [6] to direct electrical injection would remove the need for a separate pump laser, pump laser drivers/temperature controllers, and the dichroic optical splitter, which dramatically reduces the size and cost of the light source.

Although electrically-pumped MEMS-VCSELs at 1550 nm have been previously developed [9], [10], the first electrically-pumped MEMS-VCSEL at 1050 nm, suitable for ophthalmic OCT, was demonstrated by Ansbaek *et al.* in 2013 with 24 nm of tuning using a high-contrast grating mirror [11], [12]. In this paper we present an improvement in performance to 63.8 nm tuning bandwidth, coherence length measurements, and demonstration of ophthalmic OCT imaging and OCTA with the electrically-pumped source.

II. DEVICE DESIGN

The lasing cavity, schematically illustrated in Fig. 1, is comprised of a movable top mirror, air gap, multiple quantum well (MQW) gain region, and finally a fully oxidized back mirror.
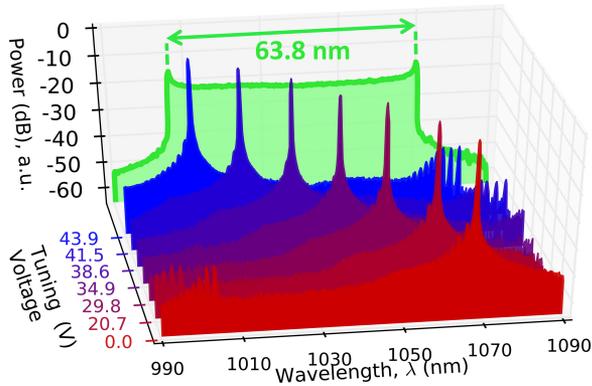
Fig. 2.   Statically- and dynamically-tuned spectra, showing 58.8 nm of static tuning and 63.8 nm of dynamic tuning. Peak wavelengths are shown in Fig. 3.

Fig. 3.   (a) Static tuning via applied MEMS tuning voltage for $I_{\mathrm{INJ}} = 2.5$ mA. (b) Three L–I–V curves obtained at different peak wavelengths for a laser packaged with SMF and FC/APC connectorized.

The MEMS portion and back mirror of the electrically pumped device follow that of our previous optically pumped MEMS-VCSELs [6]. The top mirror, a wide-band distributed Bragg reflector (DBR), is suspended over an air gap that is electrostatically adjustable via an applied tuning voltage across the top and bottom actuator contacts. Electrostatic contraction of the air gap consequently decreases the resonance wavelength of the Fabry–Pérot cavity mode, and thus the lasing wavelength.

Electrical injection is accomplished using a standard p-i-n diode structure with a p-type GaAs contact layer (at the semiconductor surface) and three intrinsic InGaAs quantum wells grown on top of an n-type GaAs/AlGaAs DBR stack (subsequently oxidized to form GaAs/Al$_x$O$_y$), on an n-type GaAs substrate. Electrical current is funneled through an oxidized current aperture, formed by partially oxidizing a p-AlGaAs layer, as is commonly used in communications VCSELs. The current subsequently provides optical gain in the MQW layers and proceeds around the fully oxidized GaAs/Al$_x$O$_y$ back-DBR mirror to the n-type backside contact. The semiconductor surface in the field, away from the optical path, is made insulating via a proton implant. Electrical injection utilizes the bottom MEMS tuning contact (at the p-type semiconductor surface) and an n-type back-side broad-area contact, with the bottom tuning contact common for both bipolar MEMS tuning and the current injection anode. Since the two MEMS tuning contacts are electrically isolated by the very high resistance air-gap, the ac tuning voltage does not produce any appreciable crosstalk in the dc injection current.

III. ELECTRO-OPTIC AND TUNING CHARACTERISTICS

The initial lasing wavelength of a representative device with no tuning voltage (V_{TUNE}) applied is $\lambda_{0\,\mathrm{V}} = 1067.0$ nm, as shown in the red 0.0 V curve of Fig. 2. The cavity was designed such that $\lambda_{0\,\mathrm{V}}$ would be very close to the point at which a second longitudinal (Fabry–Pérot cavity) mode, separated in wavelength by the cavity free spectral range (FSR), would enter the gain and mirror bandwidths (which can be seen near 1005 nm). This ensures full tuning capability, limited only by the cavity FSR, which was conservatively designed to be $\sim$67 nm for these devices. We expect future devices to approach the wider tuning
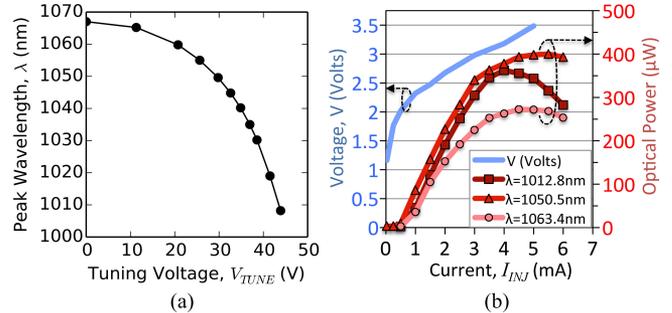
bandwidth of our previously demonstrated optically pumped designs.

The time-averaged green curve in Fig. 2 shows 63.8 nm of single-longitudinal-mode tuning (6.1% fractional wavelength tuning) at a 240 kHz sweep-rate with 59.7 V peak-to-peak tuning voltage and an injection current of $I_{\mathrm{INJ}} = 2.5$ mA. These optical spectra were collected with a 200 μm-core multi-mode fiber, which ensures the collection of higher-order lateral modes. Devices operated in a single polarization mode throughout the full tuning range, and exhibited a 300 kHz MEMS mechanical resonance frequency.

A static tuning bandwidth of 58.8 nm is shown in Fig. 3(a) for an injection current of $I_{\mathrm{INJ}} = 2.5$ mA and maximum applied voltage of 43.9 V. Fig. 3(b) shows the fiber-coupled optical power and injection voltage plotted versus injection current (I_{INJ}) for a single-mode fiber (SMF) packaged device, showing a diode turn-on voltage of 2.14 V and a forward-bias resistance of 265 Ω.

L–I curves were obtained at three different wavelengths across the tuning range, including wavelengths near the far ends of the tuning range at 1012 and 1063 nm (see Fig. 3(b)). The fiber-coupled optical power peaks at $\sim$400 μW in the center of the tuning range, and is lower at the extremes due to lowered mirror reflectivity and longitudinal mode competition at the edges. The side-mode suppression ratio (SMSR) is greater than 40 dB for I_{INJ} less than $\sim$3.0 mA; higher currents begin to exhibit side-modes and reduced SMSR, although this is partly mitigated by the SMF coupling. The small numerical aperture of SMF prevents the collection of spatially separated higher-order modes, and thus increases the SMSR while reducing the total amount of coupled optical power. The results presented in the following sections of this paper use similarly SMF-packaged MEMS-VCSELs.

IV. COHERENCE LENGTH MEASUREMENT

A distinguishing property of MEMS-VCSELs relative to other SS-OCT swept sources is the extremely long coherence length, in part enabled by the mode-hop-free and single-mode nature of this laser source. Whereas most other light sources based on short cavities, fiber loops, and other configurations have coherence lengths of a few centimeters (see Table I of [3]), which limits the OCT imaging range, the imaging range of

the MEMS-VCSEL has been shown to be significantly longer [2]–[4]. The coherence length of the MEMS-VCSEL does not appear to observably degrade with sweep rate (up to several hundred kilohertz) because the extremely short cavity length (a few micrometers) allows adequate photon roundtrips even as the cavity length is rapidly altered.

Although the MEMS-VCSEL coherence length has been demonstrated to exceed 1 m [4], previous measurements have been limited by the acquisition speed of the electronics used, and the ultimate coherence length of the MEMS-VCSEL has thus far remained unknown. This section presents what we believe are the first non-detection-limited measurements of this coherence length. First, we will briefly describe some of the theory in order to elucidate the differences between MEMS-VCSEL coherence length measurements and those of traditional solid-state diode lasers. Numerous thorough derivations of these measurements can be found in the literature [13]–[17] so the analysis shown here will simply be used to develop a background for explaining the results obtained.

In traditional solid-state semiconductor lasers, the coherence length, L_C, is commonly characterized by measuring laser linewidth, Δv, using a technique such as the self-heterodyne method [13], [14] and subsequently relating it to coherence length through the simple equation [18]

$$L_C = 0.44 \frac{c}{\Delta v}. \tag{1}$$

Equation (1) is valid for a Gaussian lineshape, and is therefore approximate in this case. However, Eq. (1) introduces pitfalls when applied to MEMS-VCSELs. This is because MEMS-VCSELs experience linewidth broadening when measured over long time scales, due to thermally-induced Brownian motion of the suspended membrane [15]–[17]. Thermal noise in MEMS has been well studied, as it is often the limiting noise source in vibrational MEMS sensors [19], [20]. These previous studies help elucidate the importance of the measurement timescale, as described below.

In the case where the measurement is made over an infinite amount of time (thereby capturing all low-frequency noise), the root mean square of the MEMS actuator motion, x_{rms}, is described by Eq. (2) [15], [16]

$$x_{rms}^2 = \frac{1}{2\pi} \int_{-\infty}^{\infty} f_n^2 \left| H^2(j\omega) \right| d\omega. \tag{2}$$

Here the motion of the MEMS actuator is found by integrating the thermal noise force, f_n, as shaped by the transfer function of the MEMS resonator, $H(j\omega)$. $H(j\omega)$ is the second order transfer function of a resonator which is readily measured experimentally. The timescale over which the noise is captured, what we will call the "integration time", is determined by the limits of the integral with time, τ, inversely proportional to angular frequency as so: $\tau = 2\pi/\omega$.

Since the thermal noise, f_n, is white noise, it can be considered a constant. The magnitude of f_n is found by the solving the integral of $H(j\omega)$ and then using the equipartition theorem to equate the energy in the MEMS spring, $\frac{1}{2}kx_{rms}^2$, to the thermal energy, $\frac{1}{2}K_BT$, where k is the spring stiffness, k_B is Boltzmann's constant and T is the temperature.

To develop intuition on integration time and its effect on the thermal noise broadening of the linewidth, we show equation (3), where the transfer function, $H(j\omega)$, in equation (2) is replaced by the MEMS parameters: the quality factor Q, the angular resonance frequency ω_0, the damping coefficient C, and spring stiffness k. The noise force, f_n, is replaced by the value calculated using the equipartition theorem [15]. This becomes an approximation since the frequencies being integrated are now limited to $\omega \geq \omega_k$; only those frequencies fast enough to be captured by the measurement time window, τ_k, where $\tau_k = (2\pi/\omega_k)$. Even the partial contributions of frequencies slower than those completely captured by the integration time are now not included.

$$x(\omega_k)_{rms}^2 \approx \frac{1}{\pi} \int_{\omega_k}^{\infty} 4 k_B T C \left| \left(\frac{k^{-1}\omega_0}{\omega_0^2 - \omega^2 + \frac{j\omega_0\omega}{Q}} \right)^2 \right| d\omega \tag{3}$$

This equation illustrates how the "white" thermal noise is filtered by the mechanical MEMS resonator (specifically, by its resonance frequency ω_0), along with how the integration time ($2\pi/\omega_k$) of the measurement selects how much of the thermal noise to capture. If we acquire a measurement on the same time scale as the resonance frequency, such that $\omega_k = \omega_0$, and $\tau_k = 2\pi/\omega_k = 2\pi/\omega_0$, the denominator becomes small and the captured MEMS motion is greatly accentuated. Most importantly, we can also see that for $\omega_k \gg \omega_0$ (i.e., a very short measurement time, τ_k), the captured mechanical motion due to thermal noise becomes very small.

The change in laser frequency, $\Delta\nu$, is then directly proportional to the actuator displacement, Δx, as shown in Eq. (4) [17]

$$\Delta v = -2 \frac{\Delta x \left| \Delta v_{FSR} \right|}{\lambda_0} \tag{4}$$

where Δv_{FSR} is the cavity longitudinal mode spacing. A short integration time, much faster than the Brownian motion of the actuator, reduces Δx, $\Delta\nu$ and the laser linewidth. If Δx is sufficiently small, the laser linewidth approaches the "intrinsic" limit, i.e., that due to standard semiconductor laser noise sources such as carrier and photon fluctuations. Similarly, the emitted MEMS-VCSEL beam should remain coherent at path delays corresponding to a time delay that is small compared to the resonance timescale ($2\pi/\omega_0$), enabling interferometry at longer distances than might be expected based on a MEMS-VCSEL linewidth measurement with long-integration time.

Consider a Mach–Zehnder interferometer (MZI) as shown in Fig. 4. Here the length of fiber delay, ΔL determines the integration time, i.e., the time over which wavelength fluctuations will be captured. For our typical actuator resonance frequency ($f_0 = \omega_0/2\pi$) of 300 kHz, integration timescales shorter than $\tau_k = 1/f_0 \approx 3.3\,\mu s$ will eliminate much of the Brownian-motion contribution according to Eq. (3).

For example, a fiber delay of 100 m corresponds to an optical delay time of only 480 ns, nearly an order of magnitude smaller than the timescales unfiltered by the MEMS resonance frequency, and so we might expect the laser to retain some degree of coherence at 100 m (provided other linewidth broadening mechanisms are sufficiently small, which is generally expected to be true [13]–[15], [17]). In theory, the
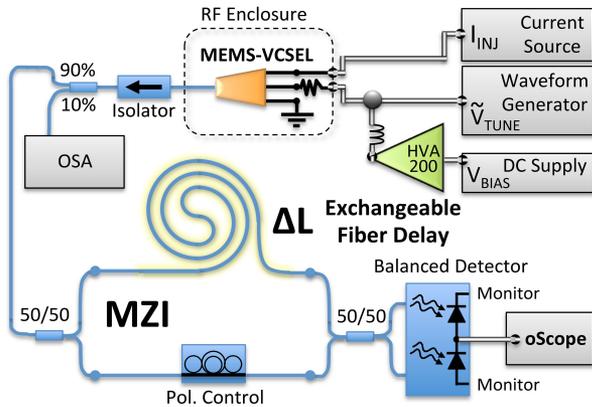
Fig. 4. Configuration of coherence length measurement. MEMS-VCSEL wavelength is swept ∼2 nm sinusoidally at 300 kHz. The fringes created by the MZI delay are fed into 1.6 GHz balanced detectors and read by a 40 GS/s real-time oscilloscope with 2.5 GHz analog front-end, while the tuning is monitored by an OSA.

Fig. 5. Interferogram fringe amplitude drops as the MZI fiber delay length is increased to 80 m. Diamonds represent the median value of 12 measurements taken at each fiber length. Inset shows the interference fringes observed for 80 m fiber delay at the end of the sweep range (slowest velocity).

self-heterodyne technique (detailed in [13] and [14]) should yield a correspondingly small linewidth, provided that the electrical spectrum analyzer (ESA) could acquire data with a measurement time of a few hundred nanoseconds, instead of the ∼1 s that is normally achievable with commercially available ESAs.

We measured the coherence length using the technique described in [13] with the experimental setup shown in Fig. 4. Rather than dynamically varying the length of one MZI arm as suggested in [13], we instead tuned the VCSEL over a small range to produce interference fringes on the oscilloscope. We define coherence length as the optical path length difference at which the measured fringe amplitude is reduced by a factor of 2. Our measurement is of the same SMF-packaged VCSEL used to produce Fig. 3(b), and with the laser driven at $I_{INJ} = 3.0$ mA, generating ∼340 μW of unamplified optical output power. The MEMS tuning voltage was driven with a 300 kHz sinusoidal voltage generated by an Agilent 33220A Arbitrary Waveform Generator, combined in a bias tee with a filtered dc bias generated by a Thorlabs HVA200 high-voltage amplifier and dc supply. We captured the interferograms with Thorlabs 1.6 GHz PDB480C-AC balanced photodetectors and acquired data with a LeCroy 2.5 GHz, 40 GS/s real-time oscilloscope.

The very long path-length differences measured here necessitated a reduction in the MEMS tuning velocity, which was accomplished by tuning over only ∼2 nm. Even with the minimized tuning range, the photodetector's 1.6 GHz cutoff frequency limited our fringe amplitude measurement to the ends of the sinusoidal sweep where the MEMS actuator motion changed direction (moved at the slowest velocity). Fringes like those shown in the inset of Fig. 5 are clearly visible with up to 80 m of fiber delay, having only dropped in amplitude by ∼30% at 80 m. Interference fringes were measured 12 times at each fiber length. Fitting a line to the fringe amplitude versus fiber delay length in Fig. 5, the 3 dB coherence length is estimated to be 150 ± 33 m in fiber (225 ± 51 m in air, using a fiber group velocity of $n_g = 1.50$).
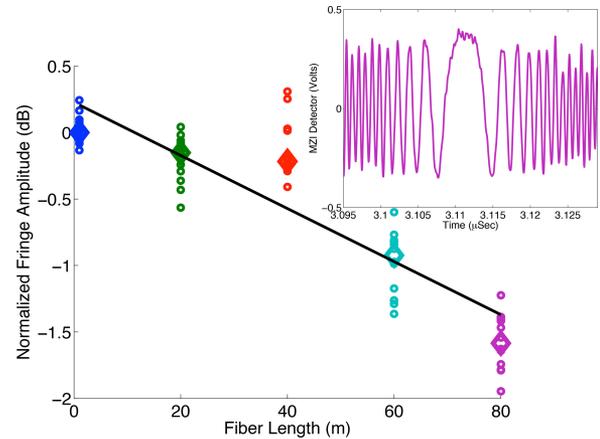
Using equation (1), the estimated coherence length of 225 m corresponds to an instantaneous linewidth on the order of ∼0.5–1.0 MHz. This value is reasonable, given that previous workers in fixed wavelength NIR VCSELs have shown 3 MHz linewidths [21], and the airgap in the MEMS-VCSEL can be expected to further narrow the linewidth.

Our measured coherence length far exceeds that required for currently envisioned SS-OCT applications, but suggests the further utility of the MEMS-VCSEL in OFDR or other distance ranging applications.

V. OPTICAL COHERENCE TOMOGRAPHY IMAGING

A similar VCSEL of the same design as described in Sections II–IV was packaged, fiber coupled, and FC-APC fiber connectorized with SMF. Fig. 6 shows a schematic diagram of the electrically pumped VCSEL light source used for SS-OCT imaging experiments. A constant current source (Thorlabs LDC201 ULN) pumped the VCSEL at 4 mA to generate laser emission. A voltage signal from the first output channel of an arbitrary waveform generator (Tektronix AFG3102) was amplified by a high voltage amplifier (Trek 2100 HF) and used to drive the electrostatic MEMS tuning mechanism in the VCSEL with a 400 kHz sine wave from ∼43 to ∼56 V. The fiber-coupled optical output power of the VCSEL during the wavelength sweep was ∼183.5 μW in each sweep direction (367 μW total), therefore post amplification with a booster optical amplifier (BOA) was required to reach the power levels of ∼19 mW required for OCT imaging. The BOA (Praevium, Inc. and Thorlabs Quantum Electronics) was a prototype wide bandwidth and high gain design developed specifically for 1050 nm swept source VCSEL applications. A broad bandwidth 1050 nm optical isolator (DPM Photonics) was placed between the VCSEL and BOA to prevent amplified spontaneous emission from the BOA and back-reflections from the OCT instrument reaching the VCSEL. Polarization controllers (PC) were placed before the isolator to align the VCSEL light polarization state with the isolator and before the BOA to align the VCSEL light polarization state to
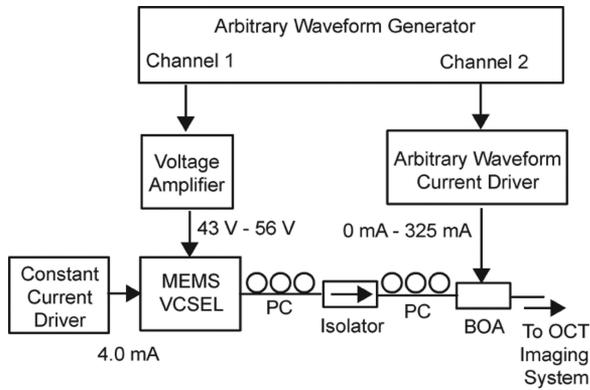
Fig. 6. Schematic diagram of the VCSEL light source used for OCT.

Fig. 7. (a) Interferometric fringe measured directly from VCSEL. (b) Interferometric fringe with 325 mA constant-current driven BOA amplifying the VCSEL. (c) Arbitrary current waveform used to drive the BOA for spectral shaping. (d) Interferometric fringe from spectrally shaped BOA amplifying the VCSEL. (e) OCT point spread function on linear scale. (f) OCT point spread function on log scale. (g) Time-averaged optical spectra from constant current driven BOA and current shaped BOA configurations. Arrow indicates FBG location.

the BOA. Channel 2 of the arbitrary waveform generator was connected to a prototype high speed 11.5 MHz bandwidth BOA current driver (Thorlabs, Inc.). The BOA was driven with an arbitrary waveform current profile in order to preferentially shape the emission spectra for improved OCT imaging performance and to blank the forwards laser sweep. The output of the BOA was then used as the input to a phase stabilized OCT imaging system, similar to that described in reference [7], but with an upgraded analog-to-digital converter (ADC) digitizer board (Alazar ATS9360 $+/-$ 400 mV input range) which allowed optical clocking at $\sim$930 MSPS and with a fiber Bragg grating (FBG) positioned at 1065.2 nm. Phase stabilization in this work improves the performance of the background subtraction step in the OCT processing to reduce fixed pattern noise in the OCT intensity image [7]. Fixed pattern noise can cause errors in the speckle variance calculation of the OCTA processing, especially if there is motion of the eye relative to the imaging instrument.

Fig. 7(a) shows example fringes obtained from the unamplified VCSEL, which are the interferograms resulting from digitizing the output signal of a dispersion balanced MZI during the VCSEL sweep. The fringes include a forward (short to long wavelength) and backward (long to short wavelength) sweep as the MEMS mirror in the laser cavity oscillates. Applying a constant 325 mA current to the BOA during the backwards sweep and turning the BOA off during the forwards sweep generates a 400 kHz repetition rate unidirectional swept laser source for OCT, as shown in Fig. 7(b). The BOA amplified fringe (see Fig. 7(b)) and unamplified VCSEL fringe (see Fig. 7(a)) have similar profiles.

Fourier transforming a k-space (wavenumber) linearized OCT fringe from a sample with an isolated reflection generates an axial scan and point spread function which characterizes the axial resolution and contrast, as shown in Fig. 7(e). The point spread function has large sidelobes because of the sharp edges, rectangular shape, and non-zero amplitude value at the start and end of the fringe. Because the sidelobes appear in the OCT image and can cause confusion and misinterpretation of retinal layer boundaries, it is common to apply a sidelobe suppressing apodization function (e.g., hanning, cosine, etc.) in data processing before the Fourier transform. However, the software spectral shaping approach is suboptimal from an OCT

sensitivity perspective because it reduces signal to noise ratio (SNR).

By adjusting the drive current to the BOA as a function of time (see Fig. 7(c)) with a peak current of 325 mA, the fringe (see Fig. 7(d)) can be preferentially shaped to reduce sidelobes and make more optimal use of light exposure to improve SNR, which is critical for high speed OCT imaging applications [22]. The full width half max of the axial point spread function (see Fig. 7(e)) with the 325 mA constant current mode is 10.8 μm in air (8.1 μm in tissue assuming a refractive index of $n = 1.33$) and with the spectrally shaped current is 13.0 μm in air (9.8 μm in tissue) as measured with the MZI and an oscilloscope, using
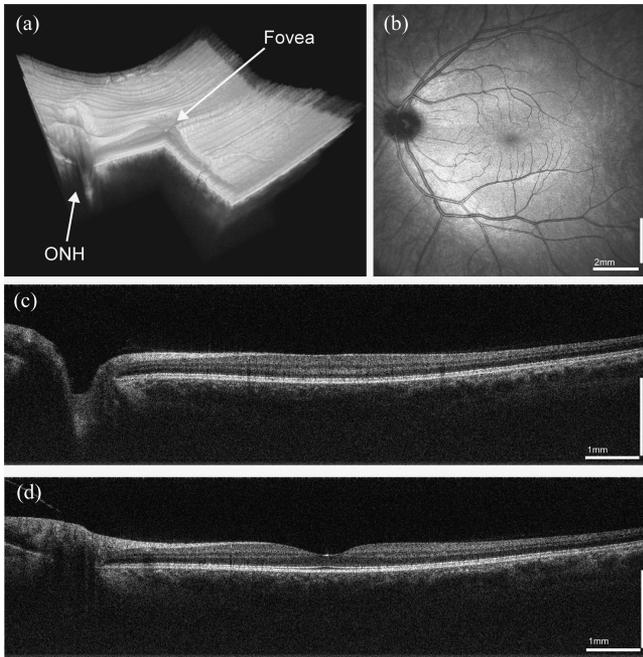
Fig. 8. (a) Wide field 3-D rendering of human retina data obtained with the VCSEL source. (b) OCT Fundus image. Scale bars are 2 mm. (c) Wide field OCT cross sectional image intersecting the optic nerve head. Scale bars are 1 mm. (d) Wide field OCT cross sectional image intersecting the fovea. Scale bars are 1 mm.

Fig. 9. (a) OCTA projection data of the human macula over 6 mm × 6 mm. (b) OCTA projection data of the human macula over 3 mm × 3 mm. (c) 3-D rendering of OCT intensity data in gray with cutaway to show OCTA data of the vasculature and capillaries in red/yellow. (d) OCT cross sectional image consisting of the average of five repeated B-scans at the fovea location. All scale bars are 1 mm.

software-linearized k calibration. The sidelobes of the spectrally shaped point spread function are reduced by about 11 dB, as shown in Fig. 7(f). A non-zero fringe amplitude at the start and end of the sweep is required for optical clocking of the ADC digitizer board.

The sidelobes could optionally be further reduced by applying software spectral shaping. We experimentally measure an approximate 2–3 dB improvement in OCT sensitivity when using the shaped fringe versus the constant current fringe (with proper light attenuation to achieve comparable exposure on the eye). The spectra for the constant current and shaped fringes, measured with an optical spectrum analyzer (OSA) are shown in Fig. 7(g).

A prototype OCT instrument was used to image a human retina. Study protocols were approved by the institutional review board of the Massachusetts Institute of Technology. Written informed consent was obtained prior to the study. Retinal imaging was performed with an incident average power of 1.8 to 1.9 mW, consistent with American National Standards Institute standards and with exposure levels used in other research OCT ophthalmic instruments at 1050 nm. The axial resolution measured from the OCT instrument with optical clocking and a dispersion compensating water cell in the reference arm was 14.3 μm in air (10.8 μm in tissue) after applying software dispersion compensation.

With 1.8 mW exposure on the eye, the measured OCT sensitivity was 97 dB for the shaped spectrum configuration (only the shaped spectrum configuration was used to acquire human retina data). The Nyquist limited imaging range of the instrument was 3.1 mm in air (2.3 mm in tissue). Previous work with optically

pumped VCSELs has shown that it is possible to image with either a single direction of laser sweep or alternating directions of laser sweeps that are interleaved in the generation of an OCT intensity image [3]. Small differences in the optical sweep or the response of the electrical clocking circuit to the different optical sweeps or sweep directions could subtly affect the OCT axial point spread function and cause artifacts or noise in the OCTA speckle variance calculation. For this reason we conservatively chose to use only one sweep direction. It may be possible to extend the imaging range of the instrument for the same peak A/D conversion rate by utilizing both sweep directions [2], [3]. Future work will investigate bidirectional sweeping methods for OCTA calculation.

A large area volumetric 3-D dataset of the human retina consisting of 1200 × 1200 A-scans over 12 mm × 12 mm was acquired at 400 000 axial scans per second, as shown in the 3-D rendering in Fig. 8(a).

An OCT fundus image generated from axially summing pixel intensity for each transverse location in the 3-D dataset is shown in Fig. 8(b). Two selected cross sectional images extracted from the 3-D dataset are shown in Fig. 8(c) and (d). These were selected to intersect the optic nerve head and fovea, respectively, but it should be noted that any cross sectional or en face image can be generated from the volumetric dataset.

OCTA is an emerging imaging technique that uses motion contrast to visualize and quantify blood circulation in tissue [23]–[26]. By acquiring multiple repeated cross sectional images (B-scans) over the same location of the retina, changes in the speckle pattern between sequential repeated B-scans can be identified to generate motion contrast from blood flow. Displaying the speckle variance in 2-D or 3-D generates an OCT angiogram which visualizes vascular structure without the need

for injected contrast agents such as fluorescein or indocyanine green. OCTA requires the acquisition of much more data than structural OCT, and the high imaging speeds of the VCSEL at 400 000 axial scans per second enable wider imaging areas or higher pixel resolution than possible at lower speeds.

OCTA of the retina was performed using a protocol of five repeated B-scans (each consisting of 500 A-scans per B-scan) at each vertical position with 500 vertical positions acquired in 3.9 s. Imaging was performed over 6 mm × 6 mm and 3 mm × 3 mm fields of view and OCTA data were processed using methods described in reference [8].

En face display of the OCTA volumetric data shows the vasculature and capillary network in the macula (see Fig 9(a)) and the foveal avascular zone can be clearly seen (see Fig. 9(b)).

Fig. 9(c) shows a hybrid 3-D rendering with OCT intensity data shown in grayscale with a cutaway to show the OCTA data in red/yellow false color. Fig. 9(d) shows an OCT cross sectional image consisting of the average of five repeated B-scans acquired at the fovea location, which increases image quality and reduces speckle.

VI. Conclusion

We have demonstrated the widest tuning electrically pumped 1050 nm MEMS-VCSEL to-date, utilizing a GaAs-based p-i-n diode structure and oxidized current aperture. The devices exhibited 63.8 nm of dynamic tuning (6% fractional wavelength tuning) and 58.8 nm of static tuning, with single-longitudinal-mode output powers up to 400 μW in SMF packaged devices. The coherence length of SMF-packaged devices was estimated to be 150 m ± 33 m in fiber (225 m ± 51 m in air), using a variable-delay MZI configuration and high-speed fringe acquisition hardware. Additionally, ophthalmic OCT imaging was performed with the electrically-pumped MEMS-VCSEL at 400 kHz a-scan rates, resulting in wide-field 12 mm × 12 mm retinal imaging, along with OCTA of the macula showing detailed retinal vasculature.

Future work will focus on further increasing the tuning range of the electrically pumped 1050 nm MEMS-VCSEL to improve axial resolution, and approach the tuning range of previously demonstrated optically pumped devices. This can be accomplished by reducing the thickness of intra-cavity current spreading layers to increase cavity FSR.

References

[1] V. Jayaraman, J. Jiang, B. Potsaid, G. Cole, J. Fujimoto, and A. Cable, "Design and performance of broadly tunable, narrow line-width, high repetition rate 1310 nm VCSELs for swept source optical coherence tomography," *Proc. SPIE*, vol. 8276, pp. 82760D-1–82670D-11, 2012.

[2] B. Potsaid, V. Jayaraman, J. G. Fujimoto, J. Jiang, P. J. S. Heim, and A. E. Cable, "MEMS tunable VCSEL light source for ultrahigh speed 60 kHz–1 MHz axial scan rate and long range centimeter class OCT imaging," *Proc. SPIE*, vol. 8213, pp. 8230M–1–8230M-8, 2012.

[3] I. Grulkowski, J. J. Liu, B. Potsaid, V. Jayaraman, C. D. Lu, J. Jiang *et al.*, "Retinal, anterior segment and full eye imaging using ultrahigh speed swept source OCT with vertical-cavity surface emitting lasers," *Biomed. Opt. Exp.*, vol. 3, pp. 2733–2751, 2012.

[4] I. Grulkowski, J. J. Liu, B. Potsaid, V. Jayaraman, J. Jiang, J. G. Fujimoto *et al.*, "High-precision, high-accuracy ultralong-range swept-source optical coherence tomography using vertical cavity surface emitting laser light source," *Opt. Lett.*, vol. 38, pp. 673–675, Mar. 1, 2013.

[5] C. D. Lu, M. F. Kraus, B. Potsaid, J. J. Liu, W. Choi, V. Jayaraman *et al.*, "Handheld ultrahigh speed swept source optical coherence tomography instrument using a MEMS scanning mirror," *Biomed. Opt. Exp.*, vol. 5, pp. 293–311, Jan. 2014.

[6] V. Jayaraman, G. D. Cole, M. Robertson, C. Burgner, D. John, A. Uddin *et al.*, "Rapidly swept, ultra-widely-tunable 1060 nm MEMS-VCSELs," *Electron. Lett.*, vol. 48, pp. 1331–1332, Oct. 2012.

[7] W. Choi, B. Potsaid, V. Jayaraman, B. Baumann, I. Grulkowski, J. J. Liu *et al.*, "Phase-sensitive swept-source optical coherence tomography imaging of the human retina with a vertical cavity surface-emitting laser light source," *Opt. Lett.*, vol. 38, pp. 338–340, Feb. 1, 2013.

[8] W. Choi, K. J. Mohler, B. Potsaid, C. D. Lu, J. J. Liu, V. Jayaraman *et al.*, "Choriocapillaris and choroidal microvasculature imaging with ultrahigh speed OCT angiography," *Plos One*, vol. 8, pp. e81499-1–e81499-8 Dec. 2013.

[9] M. S. Wu, E. C. Vail, G. S. Li, W. Yuen, and C. J. Chang-Hasnain, "Tunable micromachined vertical cavity surface emitting laser," *Electron. Lett.*, vol. 31, pp. 1671–1672, Sep. 14, 1995.

[10] T. Gruendl, K. Zogal, M. Mueller, R. D. Nagel, S. Jatta, K. Geiger *et al.*, "High-speed and high-power vertical-cavity surface-emitting lasers based on InP suitable for telecommunication and gas sensing," *Proc. SPIE*, vol. 7828, pp. 782807-1–782807-13, 2010.

[11] T. Ansbaek, I.-S. Chung, E. S. Semenova, and K. Yvind, "1060-nm tunable monolithic high index contrast subwavelength grating VCSEL," *IEEE Photon. Technol. Lett.*, vol. 25, no. 4, pp. 365–367, Feb. 15, 2013.

[12] T. Ansbaek, I. S. Chung, E. S. Semenova, O. Hansen, and K. Yvind, "Resonant MEMS tunable VCSEL," *IEEE J. Sel. Topics Quantum Electron.*, vol. 19, no. 4, art. no. 1702306, Jul./Aug. 2013.

[13] L. A. Coldren, S. W. Corzine, and M. Mashanovitch, *Diode Lasers and Photonic Integrated Circuits*, 2nd ed. Hoboken, NJ, USA: Wiley, 2012.

[14] A. Yariv, *Optical Electronics*. New York, NY, USA: Holt, Rinehart, and Winston, 1985.

[15] D. Huber, P. Corredoura, S. Lester, V. Robbins, and L. Kamas, "Reducing brownian motion in an electrostatically tunable MEMS laser," *J. Microelectromech. Syst.*, vol. 13, pp. 732–736, Oct. 2004.

[16] Y. Rao, W. J. Yang, C. Chase, M. C. Y. Huang, D. P. Worland, S. Khaleghi, M. R. Chitgarha, M. Ziyadi, A. E. Willner, and C. J. Chang-Hasnain, "Long-wavelength VCSEL using high-contrast grating," *IEEE J. Sel. Topics Quantum Electron.*, vol. 19, no. 4, art. no. 1701311, Jul./Aug. 2013.

[17] H. Halbritter, C. Sydlo, B. Kogel, F. Riemenschneider, H. L. Hartnagel, and P. Meissner, "Impact of micromechanics on the linewidth and chirp performance of MEMS-VCSELs," *IEEE J. Sel. Topics Quantum Electron.*, vol. 13, no. 2, pp. 367–373, Mar./Apr. 2007.

[18] W. Drexler and J. G. Fujimoto, *Optical Coherence Tomography Technology and Applications*. New York, NY, USA: Springer, 2008, p. 362.

[19] T. B. Gabrielson, "Mechanical-thermal noise in micromachined acoustic and vibration sensors," *IEEE Trans. Electron Devices*, vol. 40, no. 5, pp. 903–909, May 1993.

[20] C. H. Liu and T. W. Kenny, "A high-precision, wide-bandwidth micromachined tunneling accelerometer," *J. Microelectromech. Syst.*, vol. 10, pp. 425–433, Sep. 2001.

[21] F. M. di Sopra, H. P. Zappe, M. Moser, R. Hovel, H. P. Gauggel, and K. Gulden, "Near-infrared vertical-cavity surface-emitting lasers with 3-MHz linewidth," *IEEE Photon. Technol. Lett.*, vol. 11, no. 12, pp. 1533–1535, Dec. 1999.

[22] T. Klein, W. Wieser, C. M. Eigenwillig, B. R. Biedermann, and R. Huber, "Megahertz OCT for ultrawide-field retinal imaging with a 1050 nm Fourier domain mode locked laser," *Opt. Exp.*, vol. 19, pp. 3044–3062, 2011.

[23] L. An and R. K. K. Wang, "In vivo volumetric imaging of vascular perfusion within human retina and choroids with optical micro-angiography," *Opt. Exp.*, vol. 16, pp. 11 438–11 452, Jul. 2008.

[24] J. Fingler, D. Schwartz, C. H. Yang, and S. E. Fraser, "Mobility and transverse flow visualization using phase variance contrast with spectral domain optical coherence tomography," *Opt. Exp.*, vol. 15, pp. 12 636–12 653, Oct. 2007.

[25] S. Makita, Y. Hong, M. Yamanari, T. Yatagai, and Y. Yasuno, "Optical coherence angiography," *Opt. Exp.*, vol. 14, pp. 7821–7840, Aug. 2006.

[26] A. Mariampillai, B. A. Standish, E. H. Moriyama, M. Khurana, N. R. Munce, M. K. K. Leung *et al.*, "Speckle variance detection of microvasculature using swept-source optical coherence tomography," *Opt. Lett.*, vol. 33, pp. 1530–1532, Jul. 2008.

Demis D. John received the B.S. degree from the University of Massachusetts, Lowell, MA, USA, in 2005, and the M.S. and Ph.D. degrees in electrical engineering from the University of California, Santa Barbara, CA, USA, in 2007 and 2012, respectively, focusing on the development of ultralow-loss optical waveguides for photonic integrated circuits. He joined Praevium Research Inc., Santa Barbara, immediately following and is primarily focused on the development of electrically pumped light sources for OCT imaging and other applications.

Christopher B. Burgner, biography not available at the time of publication.

Benjamin Potsaid received the B.S., M.S., and Ph.D. degrees in mechanical engineering from Rensselaer Polytechnic Institute (RPI), Troy, NY, USA, in 1999, 2002, and 2005, respectively. Previously, he was at the Center for Automation Technologies and Systems at RPI and worked at NASA's Jet Propulsion Laboratory in Section 352. He is currently a Research Scientist at Thorlabs, Inc., Newton, NY, and a Visiting Scientist at the Research Laboratory of Electronics at the Massachusetts Institute of Technology, Cambridge, MA, USA. His research interests include the combination of optics, motion control, and image/data processing for developing high-performance systems and instrumentation for industrial, research, and biomedical applications.

Martin E. Robertson, biography not available at the time of publication.

Byung Kun Lee, biography not available at the time of publication.

Woo Jhon Choi, biography not available at the time of publication.

Alex E. Cable, biography not available at the time of publication.

James G. Fujimoto received the S.B., S.M., and Ph.D. degrees in electrical engineering and computer sciences (EECS) from the Massachusetts Institute of Technology (MIT), Cambridge, MA, USA. He joined the MIT Faculty in 1985 where he is an Elihu Thomson Professor of EECS. He is a Principal Investigator in the Research Laboratory of Electronics and the Department of EECS at MIT. His research interests include biomedical imaging, optical coherence tomography, advanced laser technologies, and applications in diverse areas including ophthalmology, endoscopy, cancer detection, surgical guidance, and developmental biology. He has published more than 400 journal articles, is an Editor or author of nine books, and holds numerous US patents. He is a Fellow of the National Academy of Engineering, National Academy of Science, and American Academy of Arts and Sciences. He received the 2001 Rank Prize in Optoelectronics, the 2011 Zeiss Research Award, and the 2012 Champalimaud Vision Award.

Vijaysekhar Jayaraman received the B.S. and M.S. degrees in electrical engineering from the Massachusetts Institute of Technology, Cambridge, MA, USA, in 1985, and the Ph.D. degree in electrical engineering from the University of California, Santa Barbara, CA, USA, in 1994. Since 1991, he has contributed to the development of wavelength agile and broadband optical sources and vertical cavity lasers at a variety of wavelengths. Notable early achievements include the first demonstration and early development of the sampled grating distributed Bragg reflector laser, and some of the first demonstrations of high-power room-temperature continuous-wave 1310 nm vertical cavity surface-emitting lasers. He is the Founder and Principal Investigator of Praevium Research Inc., Santa Barbara. At Praevium Research, his research interests include development of multiwavelength semiconductor lasers, broadband superluminescent diodes, semiconductor optical amplifiers, and ultrabroad tuning optically and electrically pumped MEMS-VCSELs.